

$(^{16}\text{O}, ^{14}\text{C})$ reaction on some even $N=28$ isotones

C. A. Ogilvie,* J. M. Nelson, D. Barker, S. J. Bennett, B. R. Fulton, S. D. Hoath,[†] M. C. Mannion,[‡]
P. J. Woods, L. Zybert,[§] and R. Zybert**

Department of Physics, University of Birmingham, Birmingham B15 2TT, United Kingdom

(Received 19 February 1988)

The two-proton stripping reaction $(^{16}\text{O}, ^{14}\text{C})$ has been measured on some of the even $N=28$ isotones: ^{48}Ca , ^{52}Cr at 160 MeV and ^{50}Ti , ^{54}Fe at 150 MeV bombarding energy. States of excitation up to 10 MeV have been extracted over an angular range 4° – 10° in the center-of-mass system. The angular distributions have been compared to transfer calculations that consist of both the simultaneous and successive transfer processes and were performed in exact finite range. Only the simple, $(1f_{7/2})^n$ dominated states have been analyzed to investigate whether this reaction mechanism can account for the data. The absolute magnitude of the $^{48}\text{Ca}(^{16}\text{O}, ^{14}\text{C})^{50}\text{Ti}$ ground-state reaction has been reproduced. However, the experimental and theoretical uncertainties are larger than the sensitivity to different structure descriptions of the target/residual nuclei. Therefore, we have not been able to probe the pairing correlations in the ground state of ^{50}Ti . The calculations fail to reproduce the magnitude of the transitions to other states in ^{50}Ti . Similar problems occurred for the other reactions, leading to ^{52}Cr , ^{54}Fe , and ^{56}Ni . The discrepancy ranges from a factor of 2 to nearly 30. In addition, there are phase differences between the calculations and the measured cross sections. Some systematics of the disagreement are investigated. It is suggested that the simultaneous/successive mechanism can account for the data when the transition is kinematically well matched. In cases of poor matching, inelastic/transfer mechanisms may be kinematically enhanced and contribute to the cross section with significant strength.

I. INTRODUCTION

It has been expected that two-nucleon transfer (TNT) reactions will prove to be a quantitative probe of pairing correlations in nuclei. However, there are problems with the description of both light- and heavy-ion-induced TNT reactions in that simultaneous transfer calculations are 1, 2, or more orders of magnitude smaller than the data. The attempts to remove this disagreement have been focused in two directions: (1) improvements in the calculation of the simultaneous transfer¹ and (2) the inclusion of multistep reaction mechanisms, the simplest of which is the two-step successive transfer of the nucleons.

This second approach has been applied to light-ion-induced TNT in recent years.^{2,3} Transitions via the excited states (often unbound) of the intermediate nuclei have been coherently included with the simultaneous transfer mechanism. These calculations reproduce both the magnitude of the measured cross sections and the details of the analyzing powers.

The same methodology, when applied to heavy-ion-induced TNT, has only had partial success. Feng⁴ and Takemasa⁵ calculated the combined simultaneous plus successive transfer for several $(^{16}\text{O}, ^{14}\text{C})$ and $(^{18}\text{O}, ^{16}\text{O})$ reactions. The inclusion of both mechanisms correctly predicted the magnitude of the $(^{18}\text{O}, ^{16}\text{O})$ data but failed for the $(^{16}\text{O}, ^{14}\text{C})$ reaction. The test data of the $^{48}\text{Ca}(^{16}\text{O}, ^{14}\text{C})^{50}\text{Ti}$ ground-state reaction at 56 MeV (Ref. 6) has been consistently underpredicted by factors of 20–30.^{4,5}

It is possible that other reaction mechanisms, e.g., inelastic processes coupled with transfer steps, significantly

contribute to the measured cross section. Some of these reaction mechanisms may be kinematically enhanced in the mismatched $(^{16}\text{O}, ^{14}\text{C})$ reaction, while remaining small in the well-matched two-neutron transfer.

If this is the case, then the $(^{16}\text{O}, ^{14}\text{C})$ magnitude discrepancy could be resolved by either extending the calculation to include further reaction mechanisms, or by remeasuring the reaction in an experimental region where it is kinematically better matched. The second approach is followed by this work, in which we describe the two-proton stripping reaction $(^{16}\text{O}, ^{14}\text{C})$ near 10 MeV/nucleon on the even $N=28$ isotones.

II. EXPERIMENTAL DETAILS

We have measured the cross sections of the reactions $^{48}\text{Ca}, ^{52}\text{Cr}(^{16}\text{O}, ^{14}\text{C})^{50}\text{Ti}, ^{54}\text{Fe}$ at 160 MeV and $^{50}\text{Ti}, ^{54}\text{Fe}(^{16}\text{O}, ^{14}\text{C})^{52}\text{Cr}, ^{56}\text{Ni}$ at 150 MeV. The experiments were performed at the NSF tandem, Daresbury, United Kingdom using the QMG/2 spectrometer⁷ to momentum analyze the outgoing ions. Angular distributions of transitions to states up to 10 MeV excitation energy were extracted over an angular range of 4° – 10° in the center-of-mass system. A set of five equidistant rectangular slits was used as the entrance aperture to the spectrometer with a horizontal acceptance (per slit) of 0.4° (lab).

The particles were measured by a hybrid focal-plane detector⁸ consisting of two multiwire position detectors and a series of ionization chambers that enable ion identification. Figure 1 demonstrates how ^{14}C ions were isolated in software from other particles crossing the focal plane. The overall energy resolution of the ^{14}C ions is

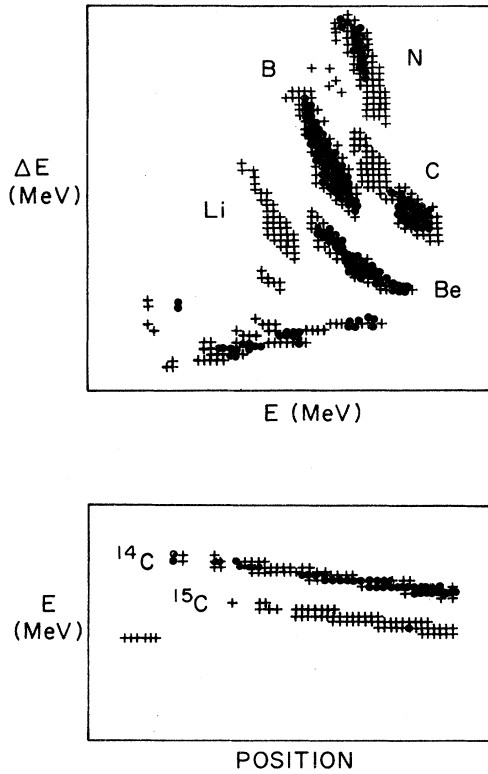


FIG. 1. The ^{14}C nuclei were isolated from other particles crossing the focal plane by gating on the carbon group in the ΔE vs E spectrum and applying a second gate in the E vs position spectrum.

listed in Table I, and a sample position spectra from the $^{48}\text{Ca}(^{16}\text{O}, ^{14}\text{C})^{50}\text{Ti}$ reaction is shown in Fig. 2.

Table I lists the thicknesses of the foils that were used, as well as the isotopic purities of the target materials. Each foil was evaporated onto a $10\text{ }\mu\text{g}/\text{cm}^2$ carbon backing. The absolute scale of the transfer cross section was established as follows. Two surface-barrier Si detectors were placed on either side of the beam in the scattering chamber to act as monitors. We measured the forward-angle elastic scattering with the spectrometer. This known cross section (Rutherford with small optical-model corrections) enabled us to determine the elastic yield into the monitors per amount of beam \times target thickness at the angles of these monitors. This monitor yield then provides the normalization for each of the reaction runs. The accuracy of this method is limited by the uncertainty of the spectrometer angle with respect to

TABLE I. The isotopic purities and target thicknesses used in this experiment, along with the experimental energy resolutions for ^{14}C ions. All targets had a $10\text{ }\mu\text{g}/\text{cm}^2$ carbon backing.

Material:	^{48}Ca	^{50}Ti	^{52}Cr	^{54}Fe
Purity (%):	97.69	96.75	99.5	95.6
Thickness ($\mu\text{g}/\text{cm}^2$):	8	40	40	60
Energy resolution (keV):	90	100	120	125

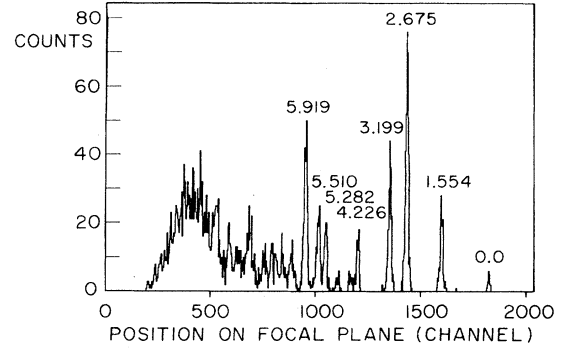


FIG. 2. A sample position spectrum of ^{14}C ions from the $^{48}\text{Ca}(^{16}\text{O}, ^{14}\text{C})^{50}\text{Ti}$ reaction at 160 MeV and at 2.8° in the lab. Several of the strong low-lying states of ^{50}Ti are indicated.

the beam axis ($\pm 0.1^\circ$), the uncertainty of the beam energy (1 part in 10^3), and the assumption of Rutherford scattering at angles near 4° (c.m.). The presence of heavy contaminants in the target provides the major problem with this method, requiring care in identification of the elastic scattering peaks in the monitor spectra. A geometric correction to the polar reaction angle due to the use of vertical slits was made, and the absolute uncertainty of the cross sections presented in this work is 20%.

III. GENERAL DESCRIPTION OF TRANSFER CALCULATIONS

Many states in the final nuclei were populated during these experiments; however, we will concentrate only on the simplest levels, those dominated by the $(1f_{7/2})^n$ configuration. If the reaction mechanism to these states

TABLE II. Bound state potential $V(r)$, where

$$V(r) = V_c(r) + V_R(r) + V(r)_{LS} 2l \cdot s$$

and

(i) $V_c(r)$ is the Coulomb potential due to a uniform, spherical charge distribution of radius R_c , where $R_c = R_{0c} A_{\text{core}}^{1/3}$,

$$(ii) V_R(r) = \frac{-V_0}{1 + \exp[(r - R_r)/a_r]},$$

where $R_r = R_{0r} A_{\text{core}}^{1/3}$;

$$(iii) V_{LS}(r) = \frac{-2.00 V_{LS} \exp[(r - R_{LS})/a_{LS}]}{ra_{LS} \{1 + \exp[(r - R_{LS})/a_{LS}]\}^2},$$

where $R_{LS} = R_{0LS} A_{\text{core}}^{1/3}$.

Parameter	Heavy nucleus	Light nucleus
R_{0r} (fm)	1.248	1.25
a_r (fm)	0.5	0.6
V_{LS} (MeV)	4.0	4.0
R_{0LS} (fm)	1.248	1.25
a_{LS} (fm)	0.5	0.6
R_{0c} (fm)	1.25	1.25

TABLE III. Comparison of the semiclassical estimates for several successive transfer routes with distorted wave (DW) calculations. The reaction is $^{48}\text{Ca}(^{16}\text{O}, ^{14}\text{C})^{50}\text{Ti}$ at 160 MeV. The semiclassical model and the DW exact-finite-range calculations (using the code FRESKO) are both described in the text. The yields are given relative to the strength of the route via the ground state of ^{49}Sc to the ground state of ^{50}Ti .

Final state ^{50}Ti J^π excitation (MeV)	Intermediate state ^{49}Sc J^π excitation (MeV)	Transfer path		Semiclassical probability (relative)	DW cross section at first maximum (relative)
		First step nlj	Second step nlj		
2^+ 1.554	$\frac{7}{2}^-$ 0.0	$1f_{7/2}$	$1f_{7/2}$	3.1	6.7
0^+ 0.0	$\frac{7}{2}^-$ 0.0	$1f_{7/2}$	$1f_{7/2}$	1.0	1.0
2^+ 1.554	$\frac{7}{2}^-$ 0.0	$1f_{7/2}$	$2p_{3/2}$	0.30	0.17
2^+ 1.554	$\frac{3}{2}^-$ 3.08	$2p_{3/2}$	$1f_{7/2}$	0.038	0.040
0^+ 0.0	$\frac{3}{2}^-$ 3.08	$2p_{3/2}$	$2p_{3/2}$	0.031	0.013
0^+ 0.0	$\frac{1}{2}^-$ 3.5	$2p_{1/2}$	$2p_{1/2}$	0.000 78	0.000 37
0^+ 0.0	$\frac{5}{2}^-$ 3.8	$1f_{5/2}$	$1f_{5/2}$	0.000 66	0.000 90

can be understood, then the structure of higher-lying states can be studied later.

Each transfer calculation presented here is the coherent addition of the simultaneous and successive transfer mechanisms, where both processes have been calculated with the same nuclear structure input (Sec. IV). The transfer calculations were performed in exact finite range using the coupled-reaction-channel code FRESKO.⁹ This code solves the coupled equations iteratively; two iterative steps being sufficient to calculate the simultaneous and successive transfer mechanisms. Microscopic form factors were generated for the simultaneous transfer by numerically transforming two single-particle eigenfunctions of a Woods-Saxon potential. This transformation involves a sum over the relative angular momentum (l) of the two nucleons; only the $l=0,1,2$ components were included, as this exhausts over 99% of the light-

nucleus form factor ($^{16}\text{O}, ^{14}\text{C}$). Both spin singlet and triplet components of the form factors have been included.

The depths of the binding potentials were adjusted to reproduce half the two-particle separation energy, while canonical values for the radial parameters (r_0, a) were used for the light nuclei (Table II). For the heavy nuclei, recent deductions of the rms radius of the proton $1f_{7/2}$ orbit in ^{51}V (Refs. 10–12) have been used to constrain the radial parameters of the heavy-nucleus Woods-Saxon (WS) potential (Table II).

For the successive transfer of two nucleons, it must be decided which intermediate states to include. As a guide to the strength of individual successive transitions, we have developed a simple semiclassical model. The model calculates the Brink probability¹³ for each transfer, adjusts the projectile energy for the second step by the Q

TABLE IV. Woods-Saxon shaped optical potentials $U(r)$, where

$$U(r) = V_c(r) + V_R(r) + iW(r)$$

and

(i) $V_c(r)$ is the Coulomb potential due to a uniform, spherical charge distribution of radius R_c , where $R_c = R_{0c}(A_T^{1/3} + A_P^{1/3})$;

$$(ii) V_R(r) = \frac{-V_{ws}}{1 + \exp[(r - R_r)/a_r]},$$

where $R_r = R_{0r}(A_T^{1/3} + A_P^{1/3})$;

$$(iii) W(r) = \frac{-W_{ws}}{1 + \exp[(r - R_i)/a_i]},$$

where $R_i = R_{0i}(A_T^{1/3} + A_P^{1/3})$.

Potential	V_{ws} (MeV)	R_{0r} (fm)	a_r (fm)	W_{ws} (MeV)	R_{0i} (fm)	a_i (fm)	R_{0c} (fm)
^{16}O (I)	100.1	1.063	0.639	24.0	1.207	0.629	1.03
^{16}O (II)	49.0	1.16	0.596	21.82	1.201	0.652	1.25
^{14}C (I)	29.59	1.252	0.590	27.99	1.212	0.548	1.25
^{14}C (II)	56.64	1.12	0.685	21.16	1.206	0.66	1.25

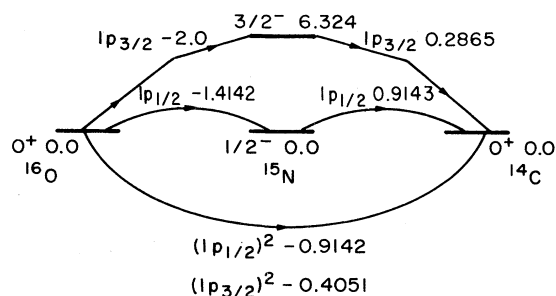


FIG. 3. The coupling diagram is comprised of the single-particle quantum numbers of each transfer along with the spectroscopic amplitudes ($CS^{1/2}$) for each reaction mechanism used in the transfer calculation. The initial, intermediate, and final states are indicated by bold lines along with their J^π and excitation energy. This diagram is for the ^{16}O , ^{15}N , ^{14}C system with spectroscopic amplitudes calculated using Cohen-Kurath matrix elements.

value of the first step, and includes a weighting factor taken from the surface part of each single-nucleon form factor. Table III lists the transfer strength predicted by the model and the exact quantum mechanical successive transfer calculation. From the approximate agreement between the two, we conclude that the model incorporates the important dynamic and structural influences in the successive transfer. We can therefore use it to predict which transitions may be excluded from the coherent, exact calculations. Note that this predicts which transitions are small, but cannot guarantee that many of these small transitions will not significantly alter the final cross section.

All successive transitions in the exact calculation were performed in the prior-post representation so that the nonorthogonality contribution is zero. The interaction

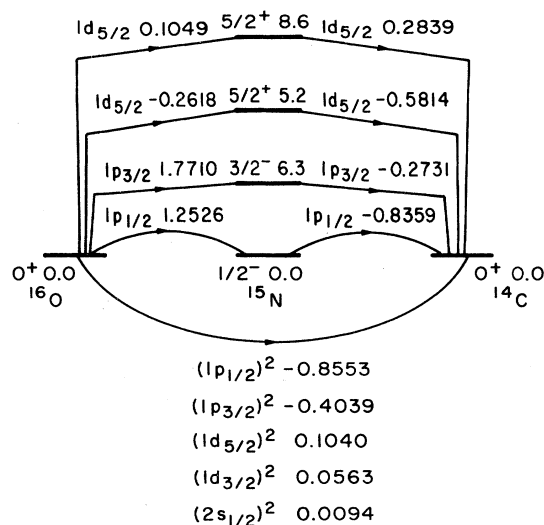


FIG. 4. As in Fig. 3, but for the ^{16}O , ^{15}N , ^{14}C system with spectroscopic amplitudes calculated using the *psd* model space.

potentials for all transfer calculations include both nuclear and Coulomb corrections to the binding interaction.¹⁴ The simultaneous transfer was calculated in the post representation with the prior representation giving similar results.

The optical-model parameters for the transfer calculations are given in Table IV. The $^{16}\text{O} + ^{48}\text{Ca}$ elastic scattering data at 160 MeV of Humanic *et al.*¹⁵ were refitted to generate the set labeled ^{16}O (II), whereas the original set is labeled ^{16}O (I). There is no available elastic scattering of ^{15}N in this mass and energy range, so the ^{16}O parameters were used. The ^{14}C optical parameters were determined from the $^{14}\text{C} + ^{50}\text{Ti}$ elastic scattering measurements at 112 MeV of Barker *et al.*¹⁶ Apart from a mass rescaling of the radius parameter, these potentials were used as the entrance, intermediate, and exit optical potentials for each reaction in this paper.

The spectroscopic amplitudes for the light nuclei (^{16}O ,

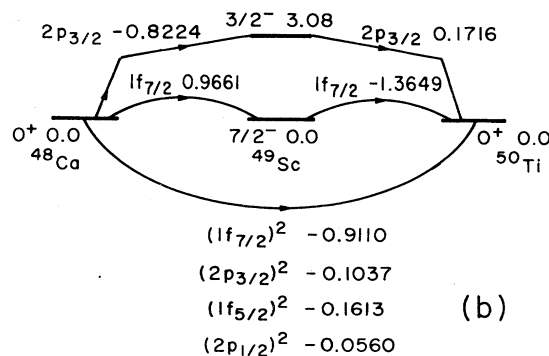
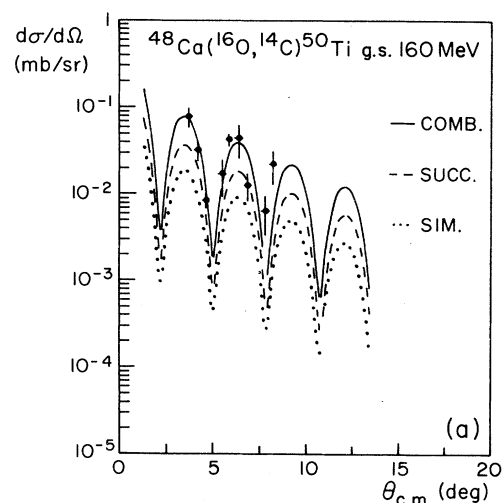


FIG. 5. (a) The angular distribution for the $^{48}\text{Ca}(^{16}\text{O}, ^{14}\text{C})^{50}\text{Ti}$ g.s. reaction at 160 MeV bombarding energy. The data are shown as circles, the full transfer calculation as a solid line, while the successive and simultaneous mechanisms are shown as a dashed and dotted line, respectively. The calculations are described in the text and have not been normalized. (b) As in Fig. 3, but for the ^{48}Ca , ^{49}Sc , ^{50}Ti g.s. system with spectroscopic amplitudes calculated using the *fp* (2p-2h) model space.

^{15}N , and ^{14}C) were calculated within the $1p$ model space using the $(8-16)\text{POT}$ interaction of Cohen and Kurath.¹⁷ As an alternative, some calculations use an extended (psd) model space with Millener-Kurath¹⁸ matrix elements. The amplitudes are listed in transfer reaction coupling diagrams; the $1p$ model space in Fig. 3 and the psd model space in Fig. 4.

IV. SHELL-MODEL CALCULATIONS $A=48-56$

Shell-model calculations in this region have demonstrated that (1) the low-energy levels of the nuclei are

dominated by the properties of the $1f_{7/2}$ configuration¹⁹ and (2) the fine details of nuclear properties (e.g., electromagnetic transition rates) often require the extension of the model space to include one-particle excitations into the $2p_{3/2}$, $1f_{5/2}$, and $2p_{1/2}$ configurations.²⁰ This is known as the fp ($1p-1h$) model space. It is conceivable that we may be able to describe part of the pairing correlations in these nuclei by extending the model space to fp ($2p-2h$) model space, i.e., up to two particles in the higher orbitals. This explicitly builds pairing correlations into the wave functions,²¹ the amount of which is dependent on the quantum numbers of the configurations (i.e., their

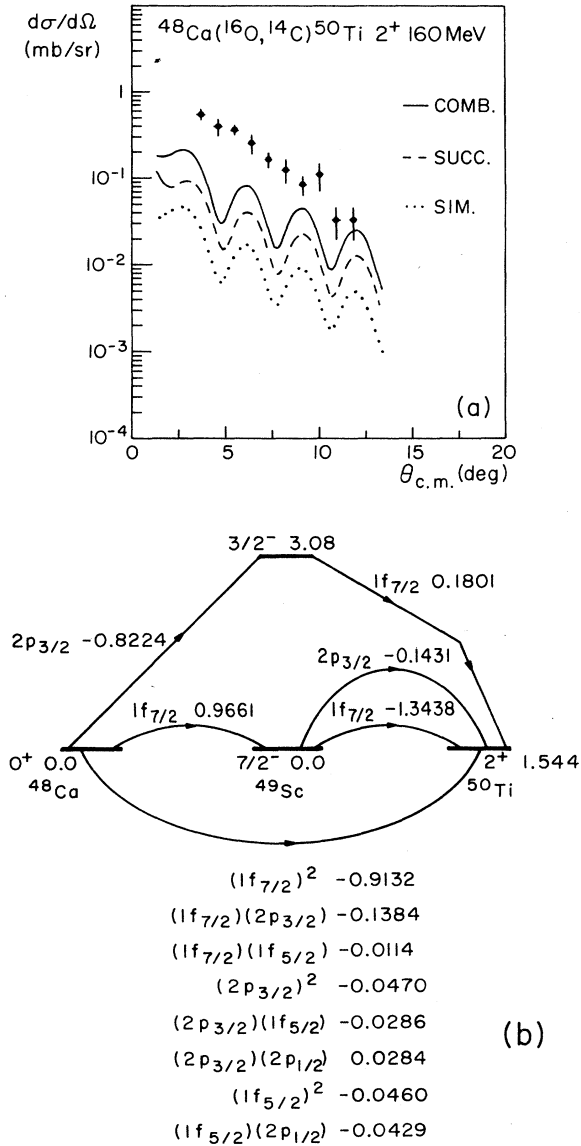


FIG. 6. (a) As in Fig. 5(a), but for the $^{48}\text{Ca}(^{16}\text{O}, ^{14}\text{C})^{50}\text{Ti } 2^+$ 1.554 MeV reaction at 160 MeV bombarding energy. (b) As in Fig. 3, but for the $^{48}\text{Ca}, ^{49}\text{Sc}, ^{50}\text{Ti } 2^+$ 1.554 MeV system with spectroscopic amplitudes calculated using the fp ($2p-2h$) model space.

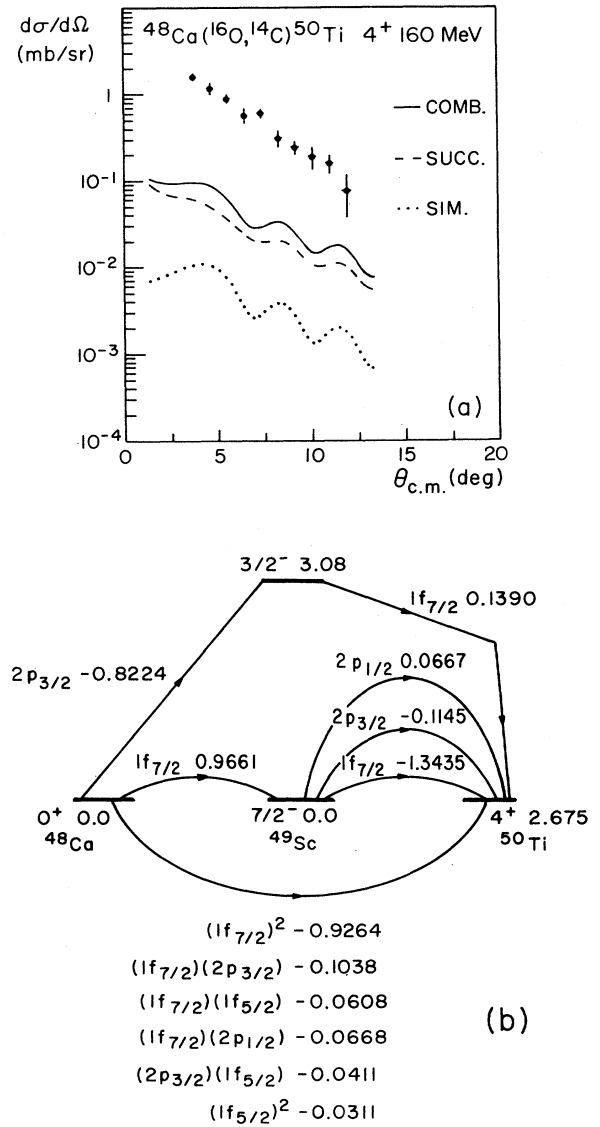


FIG. 7. (a) As in Fig. 5(a), but for the $^{48}\text{Ca}(^{16}\text{O}, ^{14}\text{C})^{50}\text{Ti } 4^+$ 2.675 MeV reaction at 160 MeV bombarding energy. (b) As in Fig. 3, but for the $^{48}\text{Ca}, ^{49}\text{Sc}, ^{50}\text{Ti } 4^+$ 2.675 MeV system with spectroscopic amplitudes calculated using the fp ($2p-2h$) model space.

geometry) and on the residual interaction present in the shell-model matrix elements.

We repeated a published set of shell-model calculations²² within the fp (2p-2h) model space. The matrix elements of this calculation are derived from Kuo-Brown matrix elements,²³ were modified by McGrory *et al.*,^{24,25} and then by Muto and Horie.²² It is not our aim to critically examine these calculations; rather we take the view that they provide us with a model estimate of the pairing correlations. If our reaction mechanism methodology proves to be reliable, then the finer details of the model's matrix elements can be examined.

We make two comments on these shell-model calculations: (1) the $1f_{7/2}$ configuration dominates the low-energy dynamics, i.e., one- and two-particle excitations typically comprise only about 20% of the state's square norm, and (2) all (2p-2h) calculations are inherently inconsistent.²⁶ States that are dominated by the 0p-0h configuration are lowered in energy through the admixture of 2p-2h components. No such effect exists for 1p-1h dominated states. This would require an extension to a 3p-3h model space. Hence the calculation predicts an energy gap of about 2 MeV between 0p-0h and 1p-1h dominated levels. Since our primary interest is with the

former levels, we will assume that this inconsistency does not effect the first-order correlated structure of the calculated wave functions. The amount of (1p-1h) component in nonzero spin states, however, may be underestimated. This will lead to weaker predictions for the successive transfer.

The shell-model calculations described in this paper have been performed with the code OXBASH (Ref. 27) and all spectroscopic amplitudes in this paper include the isospin Clebsch-Gordon coefficient. The spectroscopic amplitudes are listed in the coupling diagrams shown in the following section.

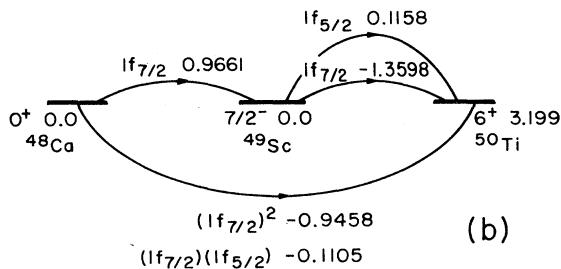
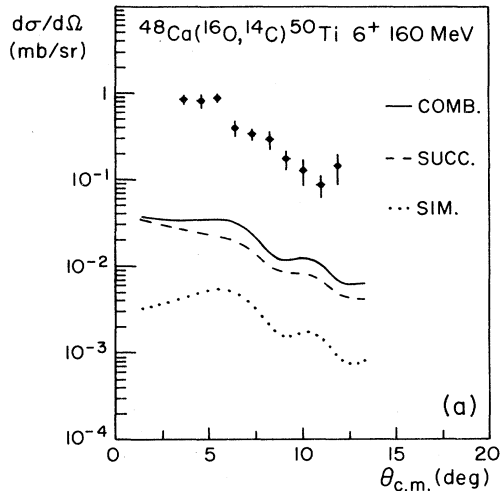


FIG. 8. (a) As in Fig. 5(a), but for the $^{48}\text{Ca}(^{16}\text{O}, ^{14}\text{C})^{50}\text{Ti}$ 6^+ 3.199 MeV reaction at 160 MeV bombarding energy. (b) As in Fig. 3, but for the $^{48}\text{Ca}, ^{49}\text{Sc}, ^{50}\text{Ti}$ 6^+ 3.199 MeV system with spectroscopic amplitudes calculated using the fp (2p-2h) model space.

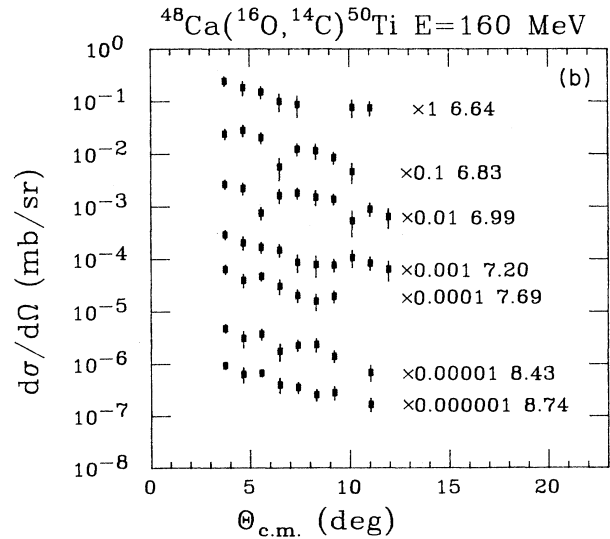
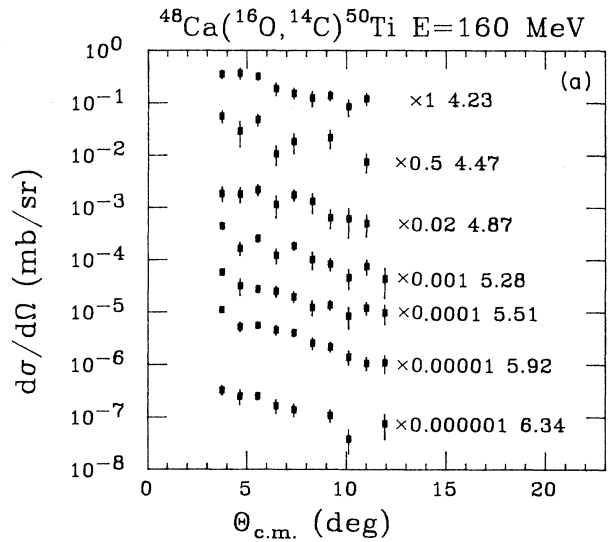


FIG. 9. The measured angular distributions for several states in ^{50}Ti populated by the $^{48}\text{Ca}(^{16}\text{O}, ^{14}\text{C})$ reaction at 160 MeV bombarding energy. The excitation energy (in MeV) of each state is adjacent to its angular distribution.

V. REACTION ANALYSIS

In this section the measured angular distributions are compared to those calculated with FRESKO. As described in Sec. III, the calculations include both simultaneous and successive transfer mechanisms. Unless stated otherwise, the $1p$ model space is used for the light nucleus, the fp ($2p-2h$) space for the heavy nucleus, and the potentials ^{16}O (I), ^{16}O (I), and ^{14}C (I) for the scattering in the entrance, intermediate, and exit channels, respectively. All calculations have been averaged over the experimental angular acceptance.

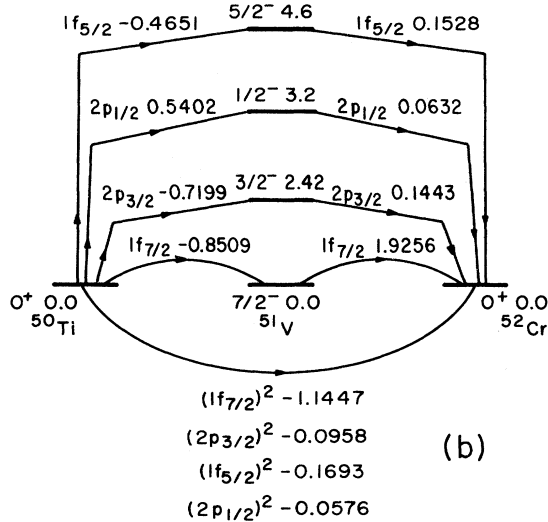
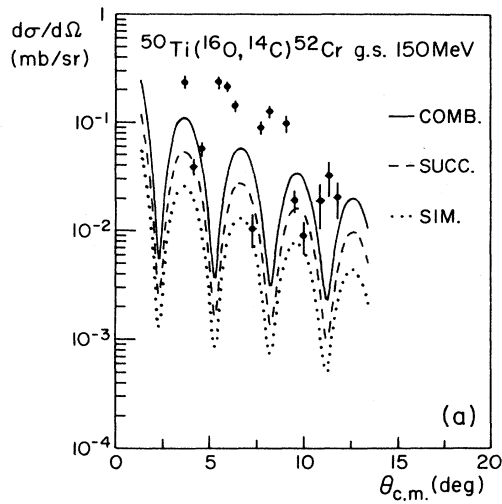


FIG. 10. (a) As in Fig. 5(a), but for the $^{50}\text{Ti}(^{16}\text{O}, ^{14}\text{C})^{52}\text{Cr}$ g.s. reaction at 150 MeV. (b) As in Fig. 3, but for the ^{50}Ti , ^{51}V , ^{52}Cr g.s. system with spectroscopic amplitudes calculated using the fp ($2p-2h$) model space.

A. $^{48}\text{Ca}(^{16}\text{O}, ^{14}\text{C})^{50}\text{Ti}$ g.s. at 160 MeV

The measured angular distribution of this reaction and the combined simultaneous/successive transfer calculation (solid line) are shown in Fig. 5(a). The calculation has not been normalized and, to our knowledge, represents the first successful description of the absolute magnitude of a two-proton transfer reaction. At this bombarding energy the successive mechanism is larger than the simultaneous transfer [Fig. 5(a)]. The coupling diagram for this calculation is shown in Fig. 5(b).

Repeating these calculations for the combinations of optical parameters given in Sec. III, a band of angular distributions is produced. The magnitude variation is about 20%, and each calculation has almost an identical shape. Using the (psd) model space for the light system reduced the magnitude of the calculation by 30%; this is largely due to the increased fragmentation of single-particle strength in ^{15}N coupled with unfavorable kinematic matching for transitions via excited ^{15}N states. Rerunning the calculations with a pure $(1f_{7/2})^n$ model space for ^{48}Ca , ^{49}Sc , and ^{50}Ti , then the cross section is smaller than that shown in Fig. 5(a) by only 10%, i.e., $N=1.10$ where $N=fp(\text{calc})/1f_{7/2}(\text{calc})$. If the simultaneous components are compared, then $N=1.45$, however, for the successive mechanism, $N=1.07$. Both enhancements are due to the extra pairing in the model wave functions;²⁸ the successive enhancement is smaller than the simultaneous enhancement because of less favorable kinematic conditions when the transfer proceeds via excited states of ^{49}Sc .

B. $^{48}\text{Ca}(^{16}\text{O}, ^{14}\text{C})^{50}\text{Ti}$ 2_1^+ , 4_1^+ , 6_1^+ states at 160 MeV

The same calculation ansatz was applied to the measured cross sections of the first 2^+ , 4^+ , and 6^+ states in ^{50}Ti . As with the ground state, these levels are dominated by the $\pi(1f_{7/2})^2$ configuration. In contrast to the success in predicting the magnitude of the ground-state reaction, the calculations underpredict the measured data by factors of 2.5 [2^+ 1.554 MeV, Fig. 6(a)], 10 [4^+ 2.675 MeV, Fig. 7(a)], and 27 [6^+ 3.199 MeV, Fig. 8(a)]. The coupling diagrams for these calculations are shown in, respectively, Figs. 6(b), 7(b), and 8(b).

The reproduction of the shape of the distributions is also poor. As with the ground state, the various combinations of optical-model parameters resulted in a band of calculations that varied in magnitude by 30%, but differed little in the shape of the distribution. Likewise, the transfer calculation that utilizes the (psd) model for the light nuclei is 30% smaller than that which uses the ($1p$) model. Comparing the calculations that utilize the $(1f_{7/2})^n$ model for the heavy nuclei to the (fp) results, the enhancements [$N=fp(\text{calc})/1f_{7/2}(\text{calc})$] are $N=1.4$, 1.1, and 1.04 for the 2_1^+ , 4_1^+ , and 6_1^+ transitions, respectively. Again the successive transfer dominates these enhancements. It is noted that in contrast to the ground state, this mechanism can now proceed by routes allowed by ($1p-1h$) components in the wave functions, such as the transfer of a $2p_{3/2}$ proton followed by that of a $1f_{7/2}$ proton.

The measured angular distributions for several other states in ^{50}Ti are shown in Figs. 9(a) and (b).

C. $^{50}\text{Ti}(^{16}\text{O}, ^{14}\text{C})^{52}\text{Cr}$ transitions at 150 MeV

The same transfer calculation methods were applied to the population of the $(1f_{7/2})^n$ dominated low-lying states of ^{52}Cr . The only significant change was that the fp (2h-2h) shell-model calculations could not be performed for states of nonzero spin in ^{52}Cr ; the matrix dimensions were too large. For these we used the spectroscopic input provided by the fp (1p-1h) shell-model calculations.²⁰

Figure 10(a) shows the measured cross section and the combined simultaneous/successive transfer calculation leading to the ground state of ^{52}Cr . The phase of the an-

gular distribution is incorrectly predicted by 1.1° , and (with this shift) is a factor of 4.4 smaller than the magnitude of the cross section. The coupling diagram for this calculation is shown in Fig. 10(b).

In a pure $(1f_{7/2})^n$ model space the seniority-two ($\nu=2$) and seniority-four ($\nu=4$) 2^+ and 4^+ states in ^{52}Cr cannot mix.²⁹ If this model space is sufficient for this nucleus, then the $\nu=4$ states (2_2^+ $E=2.965$ MeV and 4_1^+ $E=2.370$ MeV) will not be populated by the simultaneous/successive transfer mechanisms. The $\nu=2$ states (2_1^+ $E=1.434$ MeV and 4_2^+ $E=2.768$ MeV) will receive the full transfer strength. In contrast, a fp (1p-1h) shell-model calculation will mix the seniority-two and -four components. This fragments the transfer strength.

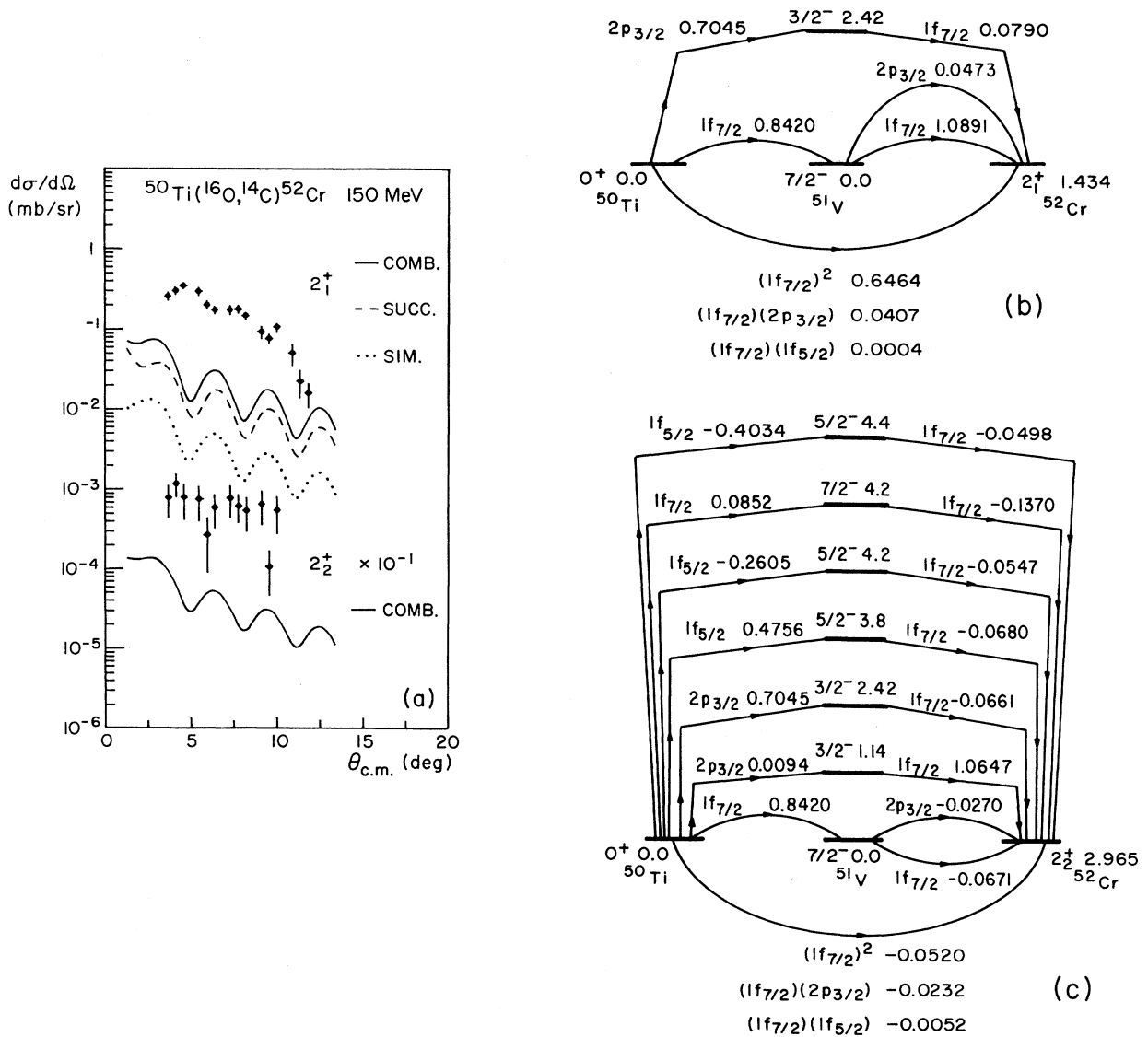


FIG. 11. (a) As in Fig. 5(a), but for the $^{50}\text{Ti}(^{16}\text{O}, ^{14}\text{C})^{52}\text{Cr}$ reaction to the 2_1^+ 1.434 MeV and 2_2^+ 2.965 MeV states at 150 MeV bombarding energy. (b) As in Fig. 3, but for the $^{50}\text{Ti}, ^{51}\text{V}, ^{52}\text{Cr}$ 2_1^+ 1.434 MeV system with spectroscopic amplitudes calculated using the fp (1p-1h) model space. (c) As in Fig. 3, but for the $^{50}\text{Ti}, ^{51}\text{V}, ^{52}\text{Cr}$ 2_2^+ 2.965 MeV system with spectroscopic amplitudes calculated using the fp (1p-1h) model space.

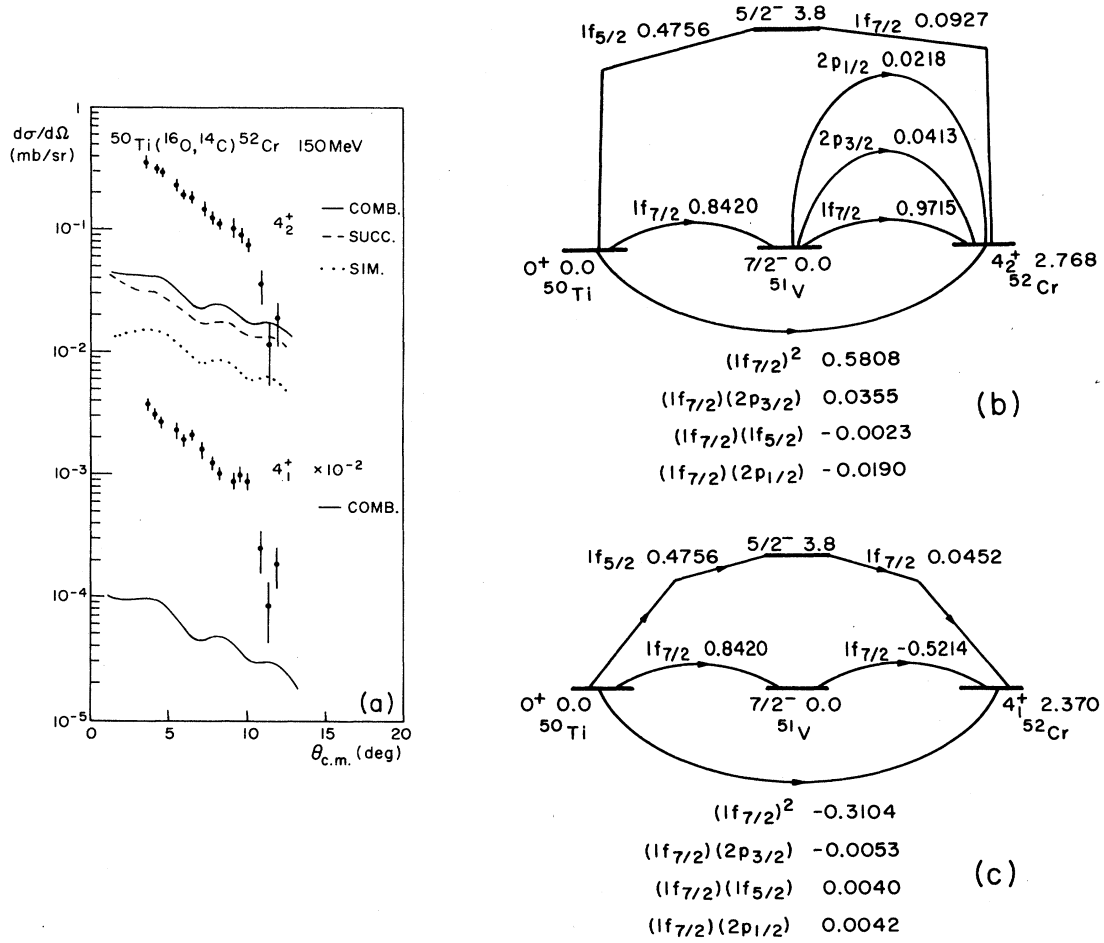


FIG. 12. (a) As in Fig. 5(a), but for the $^{50}\text{Ti}(^{16}\text{O}, ^{14}\text{C})^{52}\text{Cr}$ reaction to the 4_2^+ 2.768 MeV and 4_1^+ 2.370 MeV states at 150 MeV bombarding energy. (b) As in Fig. 3, but for the $^{50}\text{Ti}, ^{51}\text{V}, ^{52}\text{Cr}$ 4_2^+ 2.768 MeV system with spectroscopic amplitudes calculated using the fp (1p-1h) model space. (c) As in Fig. 3, but for the $^{50}\text{Ti}, ^{51}\text{V}, ^{52}\text{Cr}$ 4_1^+ 2.370 MeV system with spectroscopic amplitudes calculated using the fp (1p-1h) model space.

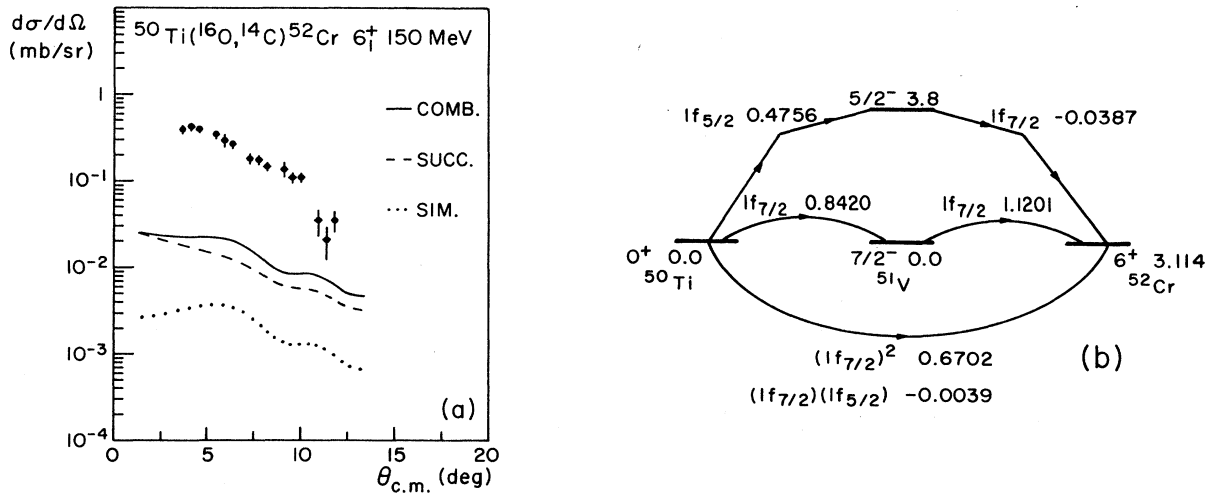


FIG. 13. (a) As in Fig. 5(a), but for the $^{50}\text{Ti}(^{16}\text{O}, ^{14}\text{C})^{52}\text{Cr}$ 6_1^+ 3.114 MeV reaction at 150 MeV bombarding energy. (b) As in Fig. 3, but for the $^{50}\text{Ti}, ^{51}\text{V}, ^{52}\text{Cr}$ 6_1^+ 3.114 MeV system with spectroscopic amplitudes calculated using the fp (1p-1h) model space.

Figure 11(a) plots the cross sections to the 2_1^+ and 2_2^+ states in ^{52}Cr . Both are underpredicted by the simultaneous/successive calculation. Qualitatively the small cross section to the 2_2^+ state indicates that it has retained a relatively pure $\nu=4$ configuration. The coupling diagrams are shown in Figs. 11(b) and (c), respectively. Figure 12(a) plots the cross sections to the 4_2^+ and 4_1^+ states in ^{52}Cr , while the coupling diagrams are shown in Figs. 12(b) and (c), respectively. Again both are underpredicted by the simultaneous/successive calculation. Qualitatively the size of the cross sections indicates that the $\nu=2$ and $\nu=4$ configurations are significantly present in both 4^+ states. However, the level of disagreement with the data is such that we are not able to assess whether the fp (1p-1h) shell-model calculation provides an ac-

curate level of this configuration mixing.

The measured angular distribution to the 6_1^+ state at 3.114 MeV and its associated transfer calculations are shown in Fig. 13(a). Again the cross section is underpredicted. The coupling diagram is shown in Fig. 13(b).

The measured angular distributions for several other states in ^{52}Cr are shown in Figs. 14(a) and (b).

D. $^{52}\text{Cr}(^{16}\text{O}, ^{14}\text{C})^{54}\text{Fe}$ transitions at 160 MeV

Applying similar calculations to the population of the low-lying levels of ^{54}Fe leads to the problems that were encountered in the preceding sections. Again due to the size of the shell-model fp (2p-2h) space (the dimensions of ^{53}Mn were too large), the spectroscopic amplitudes were taken from the fp (1p-1h) calculation.

Figure 15(a) compares the measured ground-state cross section with the combined simultaneous/successive calculation. The calculation underpredicts the data by a factor of 3.6 and is out of phase by 0.6° . The coupling diagram is shown in Fig. 15(b). The measured transitions to the 2^+ at 1.408 MeV, 4^+ at 2.538 MeV (see later in this section), and 6^+ at 2.950 MeV are each underpredicted by the corresponding combined transfer calculations. This is demonstrated in Fig. 16(a), along with the respec-

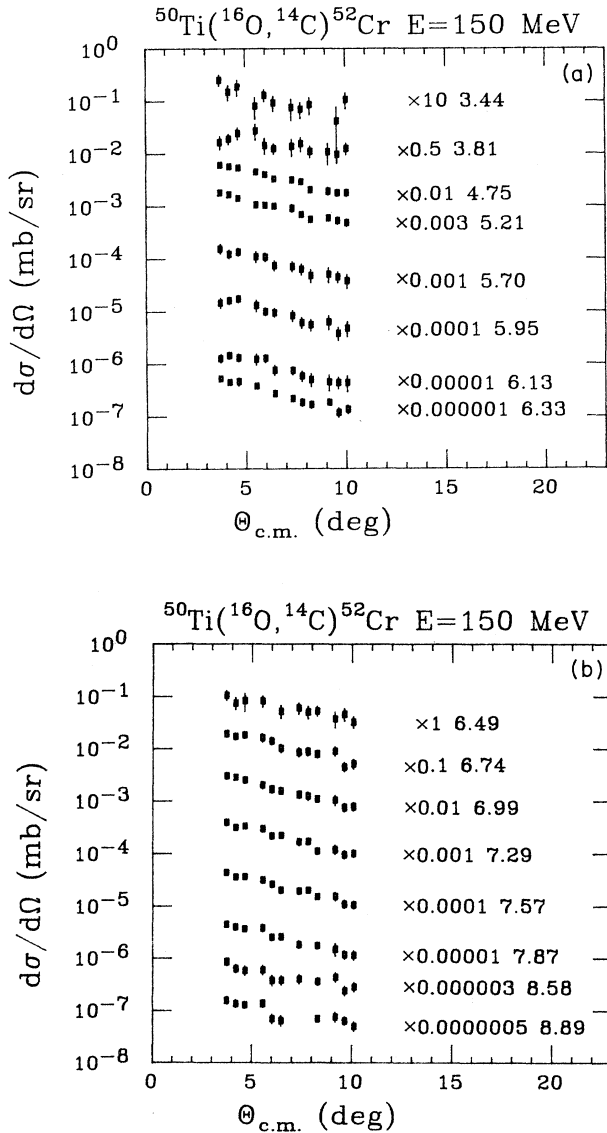


FIG. 14. As in Fig. 9, but for states in ^{52}Cr populated by the $^{50}\text{Ti}(^{16}\text{O}, ^{14}\text{C})$ reaction at 150 MeV bombarding energy.

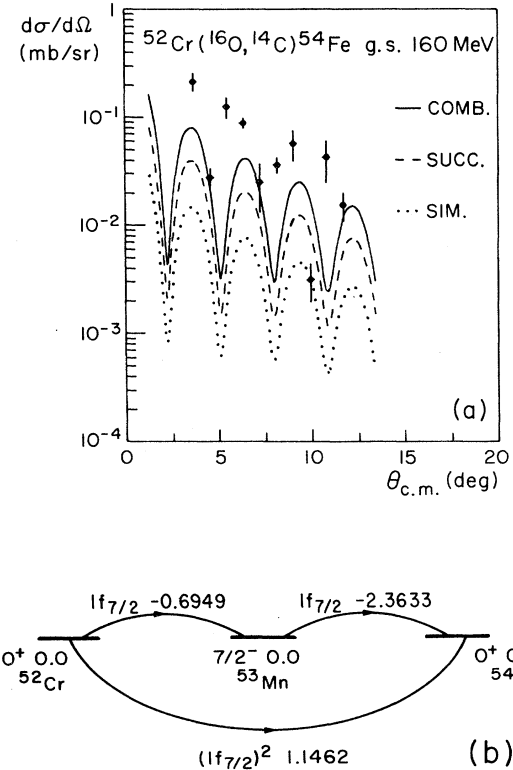


FIG. 15. (a) As in Fig. 5(a), but for the $^{52}\text{Cr}(^{16}\text{O}, ^{14}\text{C})^{54}\text{Fe}$ g.s. reaction at 160 MeV bombarding energy. (b) As in Fig. 3, but for the $^{52}\text{Cr}, ^{53}\text{Mn}, ^{54}\text{Fe}$ g.s. system with spectroscopic amplitudes calculated using the fp (1p-1h) model space.

tive coupling diagrams in Figs. 16(b), (c), and (d).

The measured transition to the 4^+ state at 2.538 MeV includes the data from the unresolved first excited 0^+ state at 2.561 MeV. We performed a least-squares fit of the $4^+/0^+$ doublet by assuming that the transitions to the 0^+ ground state and the clearly resolved 4^+ level at 3.834 MeV have typically shaped angular distributions. From this it is estimated that the 0^+ 2.561 MeV level

contributes only 5% towards the measured transition strength of the doublet.

The angular distributions for several other states of ^{54}Fe are shown in Figs. 17(a) and (b).

E. $^{54}\text{Fe}(^{16}\text{O}, ^{14}\text{C})^{56}\text{Ni}$ ground-state reaction at 150 MeV

The measured angular distribution and the combined simultaneous/successive transfer calculation are shown in

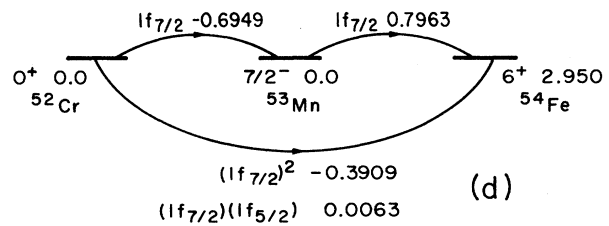
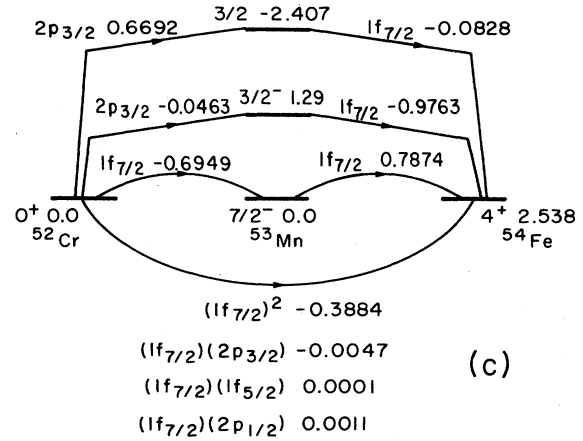
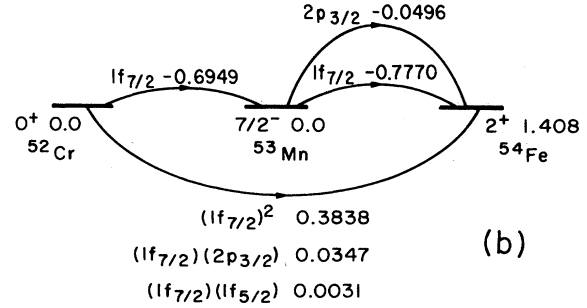
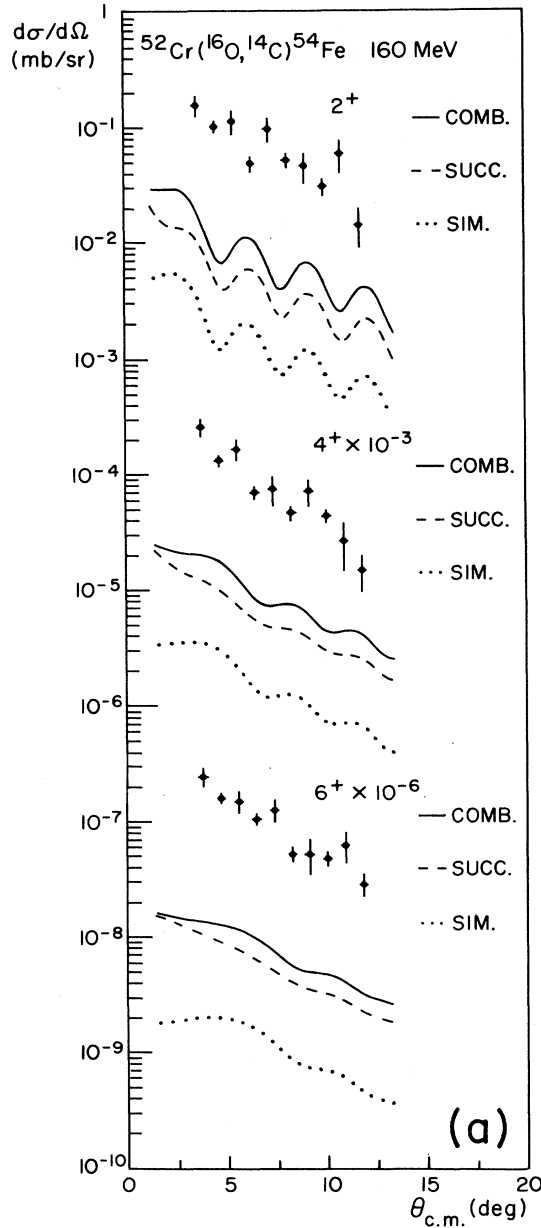


FIG. 16. (a) As in Fig. 5(a), but for the $^{52}\text{Cr}(^{16}\text{O}, ^{14}\text{C})^{54}\text{Fe}$ reaction to the 2^+ 1.408 MeV, 4^+ 2.538 MeV, and 6^+ 2.950 MeV states at 160 MeV bombarding energy. (b) As in Fig. 3, but for the $^{52}\text{Cr}, ^{53}\text{Mn}, ^{54}\text{Fe}$ 2^+ 1.408 MeV system with spectroscopic amplitudes calculated using the fp (1p-1h) model space. (c) As in Fig. 3, but for the $^{52}\text{Cr}, ^{53}\text{Mn}, ^{54}\text{Fe}$ 4^+ 2.538 MeV system with spectroscopic amplitudes calculated using the fp (1p-1h) model space. (d) As in Fig. 3, but for the $^{52}\text{Cr}, ^{53}\text{Mn}, ^{54}\text{Fe}$ 6^+ 2.950 MeV system with spectroscopic amplitudes calculated using the fp (1p-1h) model space.

Fig. 18(a). The calculation underpredicts the data by a factor of 2.9 and is out of phase by 0.9° . The coupling diagram is shown in Fig. 18(b).

The angular distributions for several other states of ^{56}Ni are shown in Fig. 19.

VI. DISCUSSION AND CONCLUSIONS

The two-proton stripping reaction ($^{16}\text{O}, ^{14}\text{C}$) has been measured on some even $N=28$ isotones (^{48}Ca , ^{50}Ti , ^{52}Cr , ^{54}Fe) at 150–160 MeV. We have attempted to describe these reactions by calculating the combined simultaneous/successive transfer mechanism. In one case, $^{48}\text{Ca}(^{16}\text{O}, ^{14}\text{C})^{50}\text{Ti}$ g.s. at 160 MeV, we have succeeded in reproducing the absolute magnitude of the cross

section. This is the first time, to our knowledge, that this has been achieved for a two-proton transfer reaction. However, the combined uncertainty of the data and transfer calculation means that we are unable to distinguish between two different shell-model descriptions of the two nuclei, ^{48}Ca and ^{50}Ti , i.e., between the $1f_{7/2}$ and fp (2p-2h) shell models.

Both simultaneous and successive transfer mechanisms are sensitive to the pairing correlations that are present in the fp model calculation. To a large extent the sensitivity in the latter mechanism is reduced by the influence of different kinematics in the intermediate channel. These effects dominate the combined transfer because, at

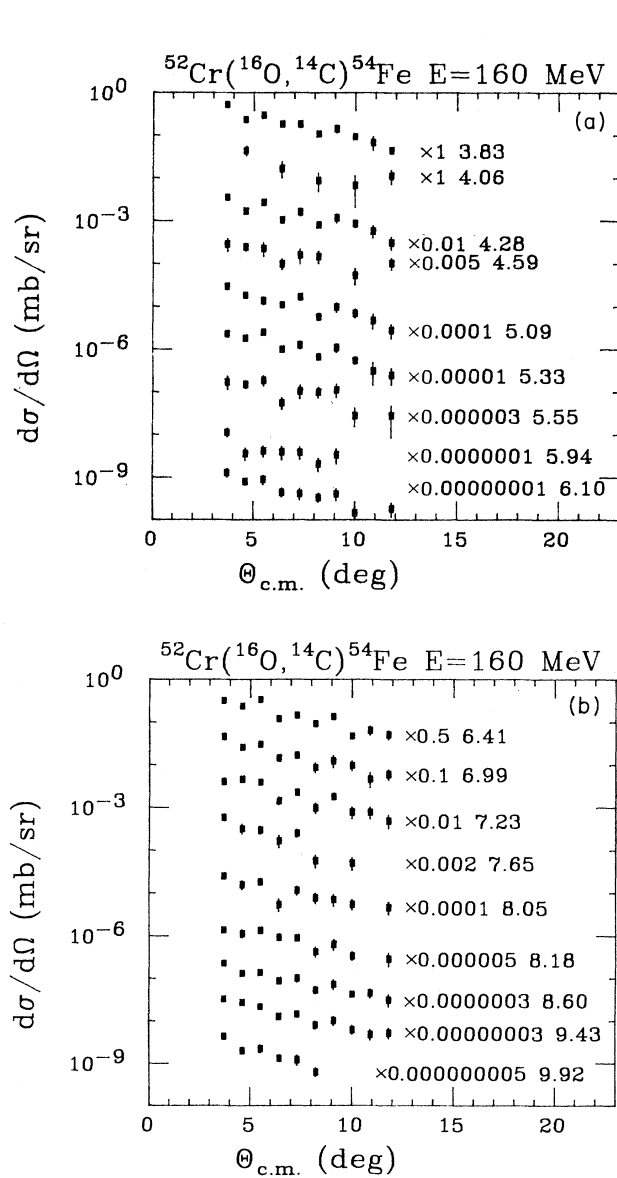


FIG. 17. As in Fig. 9, but for states in ^{54}Fe populated by the $^{52}\text{Cr}(^{16}\text{O}, ^{14}\text{C})$ reaction at 160 MeV bombarding energy.

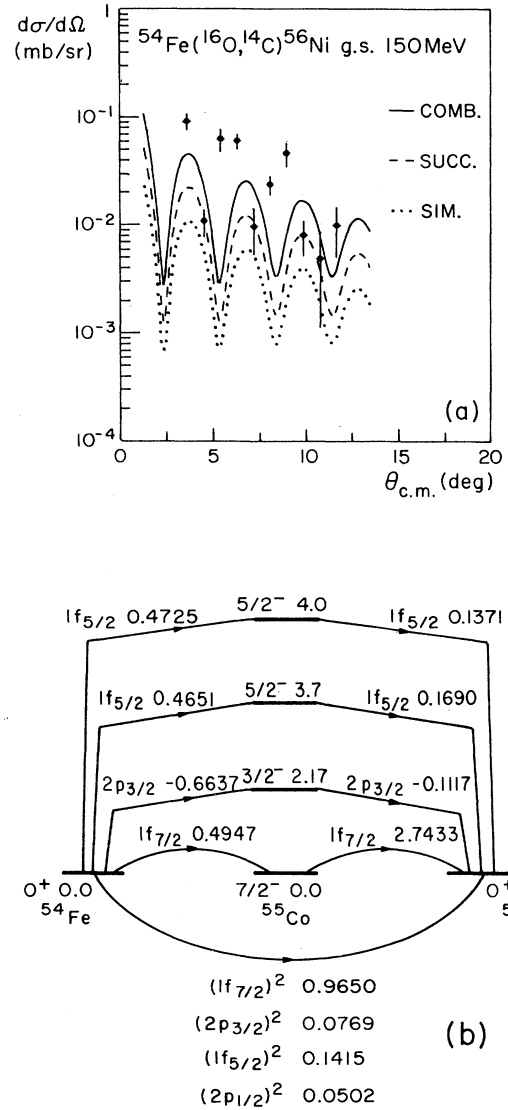


FIG. 18. (a) As in Fig. 5(a), but for the $^{54}\text{Fe}(^{16}\text{O}, ^{14}\text{C})^{56}\text{Ni}$ g.s. reaction at 150 MeV bombarding energy. (b) As in Fig. 3, but for the ^{54}Fe , ^{55}Co , ^{56}Ni g.s. system with spectroscopic amplitudes calculated using the fp (2p-2h) model space.

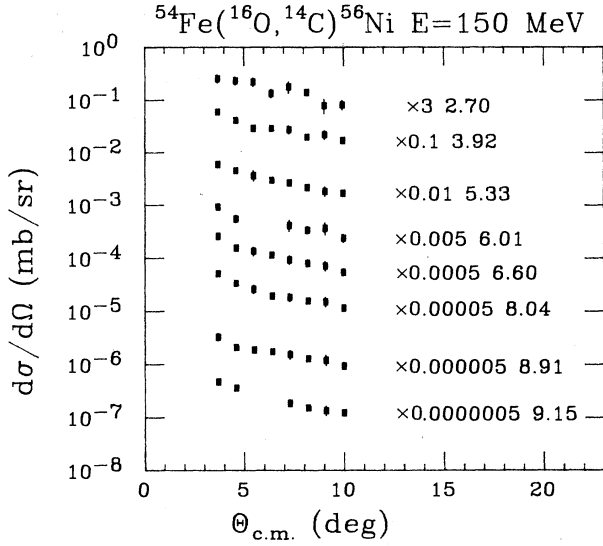


FIG. 19. As in Fig. 9, but for states in ^{56}Ni populated by the $^{54}\text{Fe}(^{16}\text{O}, ^{14}\text{C})$ reaction at 150 MeV bombarding energy.

the bombarding energy of 150–160 MeV, the successive mechanism is larger than the simultaneous transfer.

In all the other transitions that we studied, we underpredict the magnitude of the cross section and are often out of phase with the measured angular distribution by about 1° .

There are two possible, and interconnected, reasons why we failed to describe the measured transfer distributions. First, the details of the calculation, within the reaction model, could be made more realistic. For example, recent work³⁰ has succeeded in calculating the real and imaginary parts of heavy-ion optical potentials. As a trial, we used the published results³⁰ for $^{16}\text{O} + ^{40}\text{Ca}$ at 140 MeV as the entrance potential for the simultaneous transfer $^{48}\text{Ca}(^{16}\text{O}, ^{14}\text{C})^{50}\text{Ti}$ g.s. at 160 MeV. The resulting angular distribution is pulled forward, compared to previous calculations, by about 0.4° , and the magnitude is a factor of 0.7 smaller. The latter effect is due to the imaginary potential being stronger at 140 MeV as compared to 160 MeV, and the former effect is due to the imaginary potential falling steeply near the surface region, hence enhancing the contribution of higher partial waves. It is possible that by using tailor-made potentials (entrance, intermediate, exit) for each reaction system we may be able to improve the reproduction of the shape of the data.

The second possibility for the discrepancy between theory and experiment is the presence of unaccounted for reaction mechanisms, for example, inelastic couplings in the light-nucleus system, target, intermediate, or final nucleus, or any combination thereof. These may significantly populate the final state of interest.

To indirectly check the role of these mechanisms we have estimated the kinematic mismatch (ΔQ) from Brink's model of cluster transfer,³¹ $\Delta Q = Q - Q_{\text{opt}}$, where Q is the Q value of the reaction and

$$Q_{\text{opt}} = \frac{1}{2}mv^2(R_2 - R_1)/R + (Z^f z^f - Z^i z^i)e^2/R, \quad (1)$$

where m is the mass of the nucleon pair, R_1 and R_2 are the radii of the projectile and target, respectively, R is their sum, and Z and z are the charges of the targetlike and projectilelike nuclei for the final and initial channels.

For each reaction, the magnitude discrepancy between data and calculation (shifted in angle if needed) is plotted versus ΔQ . This is shown in Fig. 20. It is clear that the level of disagreement increases with increasing mismatch. This is consistent with the neglected contribution of inelastic/transfer mechanisms becoming more important when the simple routes are mismatched. Furthermore, the inelastic mechanisms may be kinematically enhanced in these cases, even if the structural overlap is small.

There is also an apparent mass dependence in the magnitude discrepancy (Fig. 20). For both successive steps in the sequential transfer, the Q value becomes more negative as the mass of the target increases. Kinematically the stripping of a proton strengthens with more negative Q values. This is likely to effect the second-step transitions from highly excited states of ^{15}N and/or the $A+1$ nucleus. These transitions have net positive Q values that become less positive as we move upwards along the isotonic chain. Hence it is possible that many weak successive transitions, via highly excited states, coherently contribute to the final transfer with more strength in the heavier isotones. Since we do not include these transitions in the calculation, this could account for the observed mass dependence in the magnitude discrepancy.

Conversely, we can understand why we have correctly predicted the magnitude of the $^{48}\text{Ca}(^{16}\text{O}, ^{14}\text{C})^{50}\text{Ti}$ g.s. reaction. The direct transfer is quite well matched, especially when compared to the earlier data at 56 MeV. This reduces the importance of inelastic/transfer mechanisms. Also the Q values for the successive steps have the largest positive values in the isotonic chain. This reduces the contribution from neglected successive transitions via highly excited states.

In the cases where fp (1p-1h) shell-model calculations

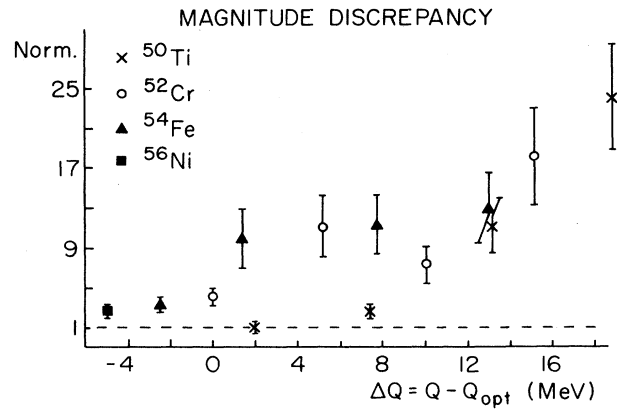


FIG. 20. The magnitude discrepancy between data and the combined simultaneous/successive transfer calculations for the reactions studied in this paper. They are plotted versus the kinematic mismatch ΔQ .

were performed, part of the underprediction could be because there is insufficient pairing in the wave functions. For the fp (2p-2h) calculations the too small amount of (1p-1h) component in the wave functions (see Sec. III) could contribute to the underprediction. From the ratio of $1f_{7/2}$ and fp (2p-2h) calculations, both of the above may increase the calculated cross section by approximately 10–30 %.

There are four main problems that currently make the ($^{16}\text{O}, ^{14}\text{C}$) reaction at this bombarding energy an unreliable spectroscopic probe.

- (1) The reaction strength is unaccounted for.
- (2) There is a subtle interplay between the kinematics, the excitation energy of the intermediate states, and the nuclear structure overlaps. This makes the use of a single reaction mechanism coupled with an overall normalization problematic.
- (3) Inelastic/transfer mechanisms are possibly important. These are likely to depend on collective as well as on pairing degrees of freedom.
- (4) It is difficult to reliably calculate the transfer, for example, optical-model uncertainties, the structure of the light system, and the problem of many small intermediate state contributions to the final reaction channel.

At lower beam energies, the matching problem is generally more severe. However, at higher energies (say 20–40 MeV/nucleon) the complicated multistep reaction mechanisms (successive and inelastic) should diminish with respect to the simultaneous transition. The Q window will also broaden, making the matching conditions less important. Hence at higher beam energies, if the simultaneous mechanism dominates all others, then the ($^{16}\text{O}, ^{14}\text{C}$) reaction may prove to be a sensitive and reliable probe of pairing correlations in nuclei.

ACKNOWLEDGMENTS

The authors acknowledge discussions held with Professor G. C. Morrison and Professor H. T. Fortune. One of the authors (C.A.O.) acknowledges the Commonwealth Association of Universities for the provision of a scholarship and three of the authors (D.B., S.J.B., and M.C.M.) acknowledge the SERC for provision of research studentships. Two of us (L.Z. and R.Z.) acknowledge the SERC for research grants. The authors would like to thank the technical crew of the Daresbury Laboratory.

*Present address: National Superconducting Cyclotron Laboratory, Michigan State University, East Lansing, MI 48824.

†Present address: Edwards High Vacuum, Crawley, Sussex, United Kingdom.

‡Present address: CEBG, Bristol, United Kingdom.

§On leave from the Institute of Nuclear Physics, Cracow, Poland.

**On leave from the Jagellonian University, Cracow, Poland.

¹J. M. Bang *et al.*, Phys. Rep. **125C**, 253 (1985).

²N. Hashimoto, Prog. Theor. Phys. **63**, 858 (1980).

³K. Yagi *et al.*, Phys. Rev. C **31**, 676 (1985).

⁴D. H. Feng *et al.*, Nucl. Phys. **A274**, 262 (1976).

⁵T. Takemasa, Nucl. Phys. **A304**, 229 (1978).

⁶Y. Eisen *et al.*, Phys. Rev. C **13**, 699 (1976).

⁷A. G. Drentje *et al.*, Nucl. Instrum. Methods **122**, 485 (1974).

⁸R. A. Cunningham *et al.*, Nucl. Instrum. Methods **234**, 67 (1985).

⁹FRESCO, I. J. Thompson, unpublished FRP version.

¹⁰S. K. Platchkov *et al.*, Phys. Rev. C **25**, 2318 (1982).

¹¹A. E. L. Dieperink *et al.*, Phys. Lett. **109B**, 2 (1982).

¹²C. A. Ogilvie *et al.* (unpublished).

¹³N. Anyass-Weiss *et al.*, Phys. Rep. **12**, 201 (1974).

¹⁴R. M. de Vries, Phys. Rev. C **11**, 2105 (1975).

¹⁵T. J. Humanic *et al.*, Phys. Rev. C **26**, 993 (1982).

¹⁶D. Barker *et al.*, Nucl. Phys. **A485**, 161 (1988).

¹⁷S. Cohen and D. Kurath, Nucl. Phys. **73**, 1 (1965).

¹⁸D. J. Millener and D. Kurath, Nucl. Phys. **A255**, 315 (1975).

¹⁹W. Kutschera *et al.*, Riv. Nuovo Cimento **1**, 1 (1978).

²⁰R. B. M. Mooy and P. W. M. Glaudemans, Z. Phys. **A 312**, 59 (1983).

²¹W. T. Pinkston, Phys. Rev. C **29**, 1123 (1984).

²²K. Muto and H. Horie, Phys. Lett. **138B**, 173 (1981).

²³T. S. Kuo and G. E. Brown, Nucl. Phys. **A114**, 241 (1968).

²⁴J. B. McGrory *et al.*, Phys. Rev. C **2**, 186 (1970).

²⁵J. B. McGrory and B. H. Wildenthal, Phys. Lett. **138B**, 173 (1981).

²⁶B. C. Metsch and P. W. M. Glaudemans, Z. Phys. **A 307**, 251 (1982).

²⁷OXBASH, A. Etchegoyen *et al.* (unpublished).

²⁸G. R. Satchler and W. T. Pinkston, Nucl. Phys. **A411**, 144 (1983).

²⁹G. Racah and I. Talmi, Physica **18**, 1097 (1952).

³⁰G. Pollaro *et al.*, Nucl. Phys. **A406**, 369 (1983).

³¹D. M. Brink, Phys. Lett. **40B**, 37 (1972).